Shape accuracy of fiber optic sensing for medical devices characterized in bench experiments

Mischa Megens[a)]
In-body Systems group, Philips Research, 5656 AE Eindhoven, The Netherlands

Merel D. Leistikow
FORS Venture, Philips - Image Guided Therapy, 5684 PC Best, The Netherlands

Anneke van Dusschoten, Martin B. van der Mark and Jeroen J. L. Horikx
In-body Systems group, Philips Research, 5656 AE Eindhoven, The Netherlands

Elbert G. van Putten
FORS Venture, Philips - Image Guided Therapy, 5684 PC Best, The Netherlands

Gert W. 't Hooft
In-body Systems group, Philips Research, 5656 AE Eindhoven, The Netherlands

(Received 2 December 2020; revised 22 March 2021; accepted for publication 23 March 2021; published 28 June 2021)

Purpose: Fiber Optic RealShape (FORS) is a new technology that visualizes the full three-dimensional shape of medical devices, such as catheters and guidewires, using an optical fiber embedded in the device. This three-dimensional shape provides guidance to clinicians during minimally invasive procedures, and enables intuitive navigation. The objective of this paper is to assess the accuracy of the FORS technology, as implemented in the current state-of-the-art Philips FORS system. The FORS system provides the shape of the entire device, including tip location and orientation. We consider all three aspects.

Methods: In bench experiments, we determined the accuracy of the location and orientation of the tip by displacing and rotating the fiber end, while allowing the rest of the fiber to change shape freely. To test the accuracy of the full shape, we have placed the fiber in a groove, which was accurately machined in a thick, stiff metal "path plate." We then compared the reconstructed shape with the known shape of the groove.

Results: The tip location is found with submillimeter accuracy, and the orientation is sensed with milliradian accuracy. The shape of a fiber in the path plate faithfully follows the known shape of the groove, with typical deviation less than 0.5 mm in the plane of the plate. Out of plane accuracy, perhaps slightly less relevant clinically, is more challenging, due to the influence of twist; yet even out of the plane, the deviation is only submillimeter.

Conclusion: The technology achieves submillimeter precision and provides full three-dimensional shape, surpassing the reported precision of other navigation and tracking technologies, and therefore may potentially alleviate the need for fluoroscopy. © *2021 Philips Research. Medical Physics published by Wiley Periodicals LLC on behalf of American Association of Physicists in Medicine* [https://doi.org/10.1002/mp.14881]

Key words: distributed optical fiber strain sensing, navigation, optical frequency domain reflectometry, radiation free, real time

1. INTRODUCTION

The progress toward minimally invasive procedures for medical interventions calls for a means of visualization of medical devices without line of sight restrictions. Traditionally, this need has been met using fluoroscopy. However, fluoroscopy relies on ionizing radiation, harmful to the patient and interventionist, and it provides a two-dimensional shadow image of the devices, making it hard to navigate within the three-dimensional anatomy. Alternatives would be desirable. Alternative navigation and tracking methods have been pursued before, notably electromagnetic (EM) tracking of the tip of a device.[1] In an optimal setting, EM tracking offers millimeter precision in tip location. However, it is affected by sources of magnetic distortion (like the presence of a C-arm), and when integrated into a medical device, the inaccuracy typically increases to multiple millimeters.[2] Fiber optics offers an alternative. Compared with EM tracking, FORS is not at all sensitive to movement of metal objects in the vicinity. Fiber optic shape sensing has been studied in the past few decades for applications ranging from mining industry to aerospace.[3] The small footprint of an optical fiber makes it an ideal sensor for incorporation into a thin medical device, such as a catheter or guidewire. With such a sensor, the shape of the device inside the human body can be determined without using harmful radiation. For almost rigid devices, such as needles, shape

sensing has been demonstrated by interpolating discrete measurement points along the device.[4] However, for long flexible devices such as guidewires, this method is insufficient since detailed information on the twist of the device is essential for accurate shape reconstruction. By measuring in a distributed fashion on submillimeter scale, it becomes possible to determine the shape of a highly flexible device accurately.[5,6]

Based on work at NASA,[7] the core technology has been further developed at Philips, initially in collaboration with Luna Innovations (Blacksburg, VA, USA) and Hansen Medical (Mountain View, CA, USA), later independently. The shape sensing technology developed at Philips, trademarked as Fiber Optic RealShape (FORS), enables real-time tracking (ca. 60 frames per second, 1 frame latency) of the full shape without line-of-sight restrictions. The shape of the device can be visualized in three dimensions, enabling intuitive navigation. This visualization provides guidance to clinicians during minimally invasive procedures. It does not require the use of ionizing radiation. It does still need an anatomical roadmap to visualize the anatomy of interest. For its initial intended use, aiding the positioning and navigation of a catheter or guidewire during endovascular procedures, creating of such a roadmap is accomplished most naturally with a digital subtraction angiogram (DSA) or coregistered preoperative computerized tomography angiography (CTA).[8] While FORS does not completely eliminate the use of radiation, it does offer great potential to reduce the cumulative radiation dose of endovascular procedures.

Originally developed with structural monitoring in mind,[9] distributed fiber optic sensing offers opportunities in biomedical applications for device tracking and treatment monitoring in minimally invasive procedures.[10] Notable early applications were in colonoscopy [11,12] and needle tracking.[13,14] These devices were based on a limited number of discrete fiber Bragg grating (FBG) sensors that act as strain gauges.[15] The differences in strain between fibers on opposite sides of a device provide a measure of local curvature. The strains can be interpolated between gratings, and for needle shape tracking, this is sufficient.[4,16–19] These devices use several fibers that are affixed inside the needle stylet, and the strains are mostly determined by the material of the needle. The alternative is to use an unattached multicore fiber that is free to move inside the device. The strain then results from the fiber material itself, and the differences in strain between gratings written in separate cores of the multicore fiber provide a measurement of local curvature.[20,21] The multicore approach simplifies the design of the device and reduces the influence of temperature and axial strain. The effect of different core configurations on the resulting curvatures has been analyzed,[19] and vectorial curvature has been measured with up to seven cores in one fiber[22] — the use of yet multiple multicore fibers[23] would seem redundant.

The aforementioned systems generally use a broadband light source and spectrometer to determine the reflection wavelength of the gratings. However, there are other possibilities. Already early on, it was shown that strains can be measured using a fiber as part of an interferometer and a scanning laser.[24,25] This technique, optical frequency domain reflectometry (OFDR), offers the opportunity to employ gratings at nominally the same wavelength; or even no fiber Bragg grating at all, instead relying on correlating the Rayleigh scattering of the fiber.[9] This approach has been patented.[5,6] It provides truly distributed sensing, rather than the discrete or quasi-distributed sensing of separate gratings.[10,26] Broadband continuous gratings can be used to enhance the signal further.[27]

For a fiber with straight fiber cores, twisting in positive or negative direction is indistinguishable: twist either way will elongate the outer cores. This can be remedied by arranging the cores in a helical fashion, as if applying a pretwist, for discrete FBGs[28] as well as OFDR.[29] For shape sensing of medical catheters and guidewires, OFDR in combination with twisted multicore fiber gratings seems most suitable. Evidently, this is not the only option: various other approaches have been put forward, such as Incoherent OFDR[30] for fiber interrogation, or employing polarization maintaining fiber for the sensors.[31] Efforts have been made to construct a single-core sensor, for example, by laser writing of waveguide couplers and FBGs in the cladding of standard single-mode fiber,[32] or utilizing tilted gratings to distinguish bending.[33] However, these approaches cannot at this time rival the quasi-continuous shape sensing with submillimeter resolution, combined with industrialized production of sensing fibers, that multicore OFDR offers.

In this article, results are presented of the first bench characterization of the FORS technology developed by Philips. We determined the precision of the location and orientation of the tip by displacing and rotating the fiber end, while allowing the rest of the fiber to change shape freely. This assessment allows for comparison to the performance of EM tracking technology. Unlike EM tracking, FORS technology provides not just the tip, but the entire shape of the fiber. To test the accuracy of the full shape, we have placed the fiber in a groove, which was accurately machined in a thick, stiff metal "path plate." We then compared the reconstructed shape with the known shape of the groove.

2. MATERIALS AND METHODS

For medical applications in the endovascular domain, the fiber shape sensor is integrated into a catheter or guidewire. We performed experiments both on bare fiber and on integrated devices. For the latter, the sensor was integrated into a 0.035" hollow flexible guidewire with an in-body section of 1.2 m. Guidewires of this diameter are used in endovascular aortic and peripheral interventions, such as endovascular aortic repair (EVAR), in which a stent graft is placed in the aneurysm region. The FORS technology currently uses an optical fiber of 190 μm outer diameter, consisting of a 125 μm cladding for the cores that guide the light, and 32 μm coating for mechanical protection. In the experiments labeled as "with bare fiber," there is no further protection outside the fiber with its coatings. In the experiments with a guidewire, the fiber is enclosed in a channel reserved for this

purpose. The fiber is free to move inside the channel, which is hermetically sealed. Since the fiber is free to move within the guidewire, no influence of the guidewire would be expected *a priori* (and this is confirmed by the experiments). Preclinical study results indicate that the fiber can be incorporated in our guidewires without adversely affecting the mechanical properties (torquability, pushability) of the devices.[8]

A laser that is part of the FORS system measures the back reflection from the fiber. The fiber has four cores, one along the central axis and three wound around it in helical fashion, see Fig. 1. Fiber Bragg gratings, which are periodic variations in refractive index, are imprinted on the cores. These gratings reflect back a fraction of the light that is sent down the cores. Bends in the fiber induce local stretching and compression of the fiber cores. The concomitant change in grating period results in a wavelength change of the grating reflection, which reveals the amount of stretching (or compression). The time delay of these reflections reveals their position along the fiber. In practice, the reflections are measured using a Fourier-domain method, that is, scanning the laser wavelength, rather than measuring the optical delay directly, an approach known as optical frequency domain reflectometry, or OFDR.[5,34,35] For the system at hand, this results in a spatial resolution along the fiber better than 50 μm. The three-dimensional shape is obtained by measuring the strains along the four cores. Differences in strain among the outer cores indicate bending; differences between the central core and the outer cores indicate twist. Strains that are common to all four cores tend to cancel out from the curvature and twist. This cancelation shields the system from influence of mechanical stress in longitudinal direction and of temperature change. The shape is reconstructed from the spatially resolved bending and twist by integrating the Frenet–Serret formulas.[36] Getting the reconstruction right requires careful attention to various details, such as nonideal fiber geometry and its associated calibration, birefringence of the fiber, and various nonlinearities, for example, in the twist; and naturally, the accuracy of a shape sensing system is constrained by finite signal to noise ratios and measurement bandwidths. This then raises the question of how accurately the technology actually can resolve the shape of a medical device. Here we focus on the accuracy of the FORS technology using nonclinical data, since this facilitates quantitative comparison with other techniques. That notwithstanding, the technology is obviously intended for clinical use. Results of a preclinical study have been published recently,[8] and first-in-human clinical study results have been presented.[37–39]

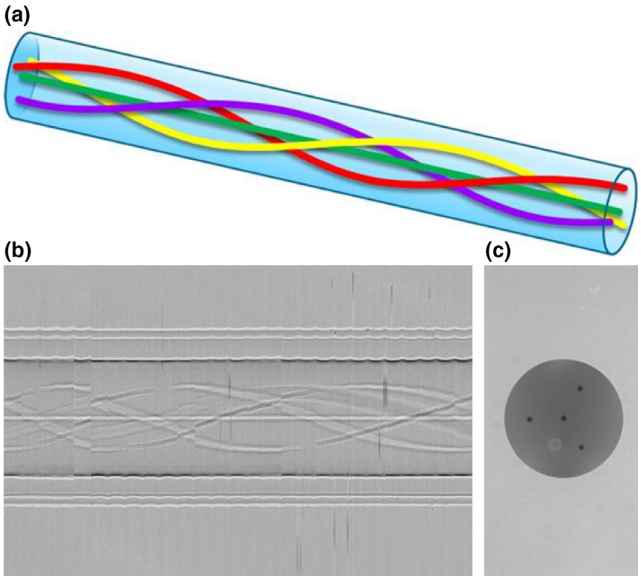

FIG. 1. Arrangement of cores in the multicore optical fiber: as a sketch (a); side view (b), microscopy, images stitched and foreshortened to show the helical twist; and in cross section (c), where the coating has been removed. The distance from central core to outer cores is 35 μm; the diameter of the cladding is 125 μm, and the total diameter, including two-layer coating, is 190 μm. [Color figure can be viewed at wileyonlinelibrary.com]

2.A. Tip positions

To determine the accuracy of the reconstructed position of the fiber tip, we have measured tip coordinates for a cubical grid of points, as illustrated in Figs. 3 and 6(a). We aim to mimic closely the protocol of Wilson et al,[40] designed for evaluation of electromagnetic (EM) tracker accuracy. The Wilson protocol involves a cube phantom of stacked cast acrylic sheets, with a 15×15 array of precisely machined holes of various depths from the top face. The EM probe is fully inserted in each hole, which provides a snug channel, and 100 samples of the probe position are recorded at each position.[40] For shape sensing, we visited the locations of the $15 \times 15 \times 15$ vertices of a Cartesian lattice on a $14 \times 14 \times 14$ cm cube, using three nominally orthogonal linear translation stages (Newport M-ILS200CC, 200PP, and 175CCHA) with an ESP-300 Motion Controller/Driver. Such stages achieve a nominal accuracy of 1.2 μm, and their accuracy is guaranteed to be better than 3.75 μm. Their pitch and yaw are guaranteed within ±100 μrad, so in combination with the short lever arm, the fiber tip should enjoy similar micron-scale positioning accuracy.

Figure 2 shows the setup. The fiber tip is clamped onto the last stage, and 50 cm ahead of the tip, the fiber is held fixed on a platform that is level with the cube (the "launch"); the fiber is otherwise free to move. The launch ensures that the fiber reconstruction starts in a well-defined position and orientation with respect to the laboratory frame; in a medical procedure, the launch is commonly situated at the side of the operating table. For each fiber tip position, 100 shapes were recorded for averaging, as in the Wilson cube phantom protocol. We have also performed measurements with the launch further away from the tip, at a distance of 1.8 m, directly on the table. Various fibers were measured; they are identified by different colors in the figures.

2.B. Registration

In the original prescription by Wilson,[40] the cube of observed tip positions is registered to the underlying lattice

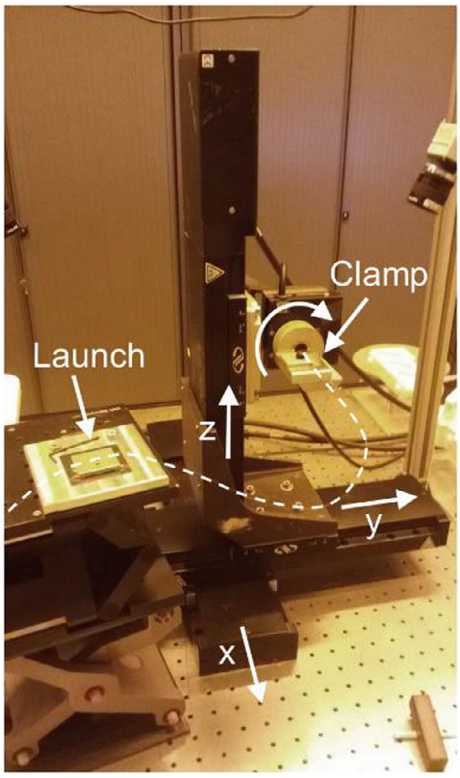

FIG. 2. Measurement setup to determine the accuracy of the position of the fiber tip. Three linear motion stages move the tip in x, y, and z direction, and a rotation stage can change the orientation of the fiber. The fiber tip is attached to the last stage by a small clamp. The fiber is attached to the table about 50 cm ahead of the tip (the "launch"). Fiber shape is reconstructed from the launch to the tip. [Color figure can be viewed at wileyonlinelibrary.com]

by selecting, in a pseudo-arbitrary manner, a set of eight to ten points in the "optimal" measurement subvolume of the system, assumed to suffer from minimal distortion, and then applying what is essentially a Procrustes transformation.[41] Here we have used a slightly different approach that allows for a slight skew between the stages, since the translation stages are bolted together by hand, presumably not perfectly at right angles; and we register with the full cube dataset. It turns out that these provisions are largely superfluous: the linear stages move as intended, and their directions are close to orthogonal. Nevertheless, we provide a brief description of the method.

We allow for an affine transformation from the lattice coordinates $(i_n\, j_n\, k_n)$ to the corresponding observed tip positions $\vec{r}_n$:

$$\vec{r}_n - \vec{r}_0 = i_n \vec{a}_1 + j_n \vec{a}_2 + k_n \vec{a}_3,$$

where the $\vec{a}_i$ are the axes of the translation stages, in the coordinate basis of the shape sensing system, and the vector $\vec{r}_0$ points from the launch to the lattice origin. The vector $\vec{r}_0$ can be dealt with straightforwardly by subtracting the mean from both the observed positions and from the lattice coordinates, that is, mean centering. The axes $\vec{a}$ then can be found using singular value decomposition (SVD).[42] Their lengths $|\vec{a}_i|$ turn out to be close to the intended lattice spacing of 10.00 mm, indeed indistinguishable within the reproducibility (of ca. 0.01 mm) among cubes. The axes are orthogonal, that is, the stages are moving in perpendicular directions, to within about 3 milliradians (0.2°) for the xy pair, and with even less skew for xz and yz. This orthogonality is quite satisfactory, considering that the translation stages are bolted together by hand; it would lead to a displacement at the edge of the cube of only 3 mrad × 140 mm / 2 = 0.2 mm. To the set of stage directions $\vec{a}_i$ corresponds a set of reciprocal vectors $\vec{b}_i$, such that $\vec{b}_i \cdot \vec{a}_j = \delta_{ij}$; multiplying a reciprocal vector $\vec{b}_i$ with the observed tip positions $\vec{r}_n$ yields the travel distances $|\vec{a}_i|\, \vec{b}_i \cdot \vec{r}_n$ of the corresponding stage i. The stage displacements are then compared with the ideal lattice to obtain a quantitative measure of the position accuracy.

2.C. Tip orientation

The Fiber Optic RealShape technology also provides information on orientation of the fiber. This can be put to use to determine the orientation of interventional devices, by attaching the fiber to the device. To quantify the orientation accuracy, we have rotated the distal end of the bare fiber, using a rotation stage (Newport SR50PP), over a range from −180° to +180°, in 5° increments. A length of 1.8 m fiber is used to accommodate the twist. Since the fiber is free hanging, it can change in shape, so in addition to the physical twist of the fiber, there is a geometrical contribution to the twist as well. Consequently, it is not sufficient to observe merely the twist measured from the helically wound fiber cores: the bending has to be taken into account too. We do this by tracking the orientation of three orthonormal vectors as we reconstruct along the fiber. The three vectors indicate the tangent to the fiber and the orientation of the outer cores. When the tip is rotated by an angle ϑ, then the three vectors at the tip rotate accordingly, tracing out circles around the rotation axis. The rotation axis can be recovered by mean centering the collection of vectors from a rotation scan, followed by SVD; the two largest SVD components are linear combinations of $\cos\vartheta$ and $\sin\vartheta$, and reveal the rotation angle ϑ. The advantage of this approach is that it is independent of the orientation of the fiber with respect to the rotation axis, that is, the fiber and rotation axis need not be collinear — in fact, the performance is better if the fiber is perpendicular to the rotation axis, as we will see below.

2.D. Path plate

The two measurements described above only refer to the tip of the fiber. The FORS technology yields not only the position and orientation of the tip but also the entire three-dimensional shape. This is helpful for navigation during minimally invasive procedures. To investigate the accuracy of the full shape, we have placed the fiber in a groove, which was accurately machined in a thick, stiff metal "path plate." We then measured coordinates of complete reconstructed shapes, and compared the reconstructed shape with the known shape of the groove. The reconstructed shapes have been registered to the known shape in the plate by cross correlating their

curvatures to find the point of entry in the groove, and then rotating and translating to minimize the distance between corresponding points, known as an orthogonal Procrustes fit.[41] The match has been further refined by locating the closest point on the groove for each measured point. The remaining distance between matching points is separated into in- and out-of-plane components.

3. RESULTS

Figure 3 shows the fiber end points for the full lattice. A few of the shapes are shown too, to provide a sense of the motion of the fiber due to the tip movement, and to show the location of the launch with respect to the cube. In Section 3.A, the jitter of the fiber tip will be discussed. This jitter is an apparent variation in the reconstructed shape, even though the sensor is physically in a fixed position. Section 3.B will cover the accuracy of the averaged sensor tip position with respect to the intended position. Section 3.C will discuss rotation sensitivity. Finally, in section 3.D we present accuracy results for full shapes.

3.A. Jitter

The recorded shapes show a slight variation in tip position, even when the stages are not moving. This "jitter" has been quantified by calculating the (co)variances of the tip coordinates. The jitter appears to be largely independent of position in the lattice. The jitter is not isotropic; it is expected to be different in the direction along the fiber, and the directions normal to and in the plane of the shape (when we consider the shape to be approximately two-dimensional). Figure 4 shows a histogram of the jitter, projected along the principal axes of the jitter ellipse, for a typical fiber. Figure 5 shows the jitter for six fibers. The jitter has a quite a pronounced anisotropy, that is, it is different along the fiber and normal to or in the plane of the shape. We will see that this can be readily understood.

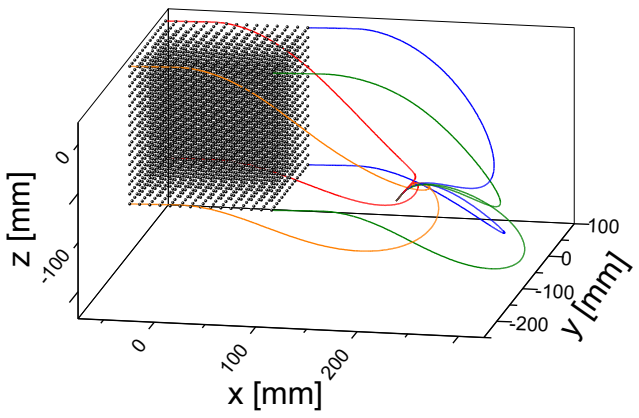

FIG. 3. Fiber tip positions for a 15 × 15 × 15 cubical grid of lattice positions spaced 10 mm apart, together with a few of the fiber shapes all the way from the launch, to provide a sense of the orientation of the lattice with respect to the launch position. The various colors serve to distinguish the fiber shapes leading to the eight corners of the lattice cube. [Color figure can be viewed at wileyonlinelibrary.com]

Figure 5 shows the jitter components in various situations, for all the fibers measured. The jitter is on a logarithmic scale, to aid in comparing the various groups. The spread in each group is similar, that is, the relative variations are about the same, and the ratios between different situations are fixed. Comparing different distances to the launch in the Figure, it appears that the jitter increases going from 50 cm to 1.8 m distance from the launch. For the fiber integrated in a device (a guidewire), we see that the jitter tends to increase slightly when integrated; however, the increase is only barely significant, the variation in the jitter among the various fibers measured is comparable to the increase in jitter upon integration.

3.B. Tip positions

The 100 measurements for each position in the lattice are averaged to obtain a tip position with reduced jitter; this facilitates the detection of even small systematic biases in tip position. Figure 6 shows the tip positions in projection. In panel a), the data are shown as measured, with a slight rotation of the axes, so the lattice points at different depths become visible, each depth with a different color. In panel b) and c), the departure from the ideal lattice is shown magnified 20×, for the same fiber (SMB0168), with the launch at 1.8 m distance in both cases, but measured with bare fiber (b) or with the fiber integrated in a device (c). The 20× magnification accentuates small distortions. Interestingly, the (small) distortion is mostly in the x, z plane, the spots from nearer and farther lattice points along the y axis line up nicely in this view. (Refer to Figs. 2 and 3 for a definition of the x, y and z directions.) By contrast, in an x, y or y, z view, the point clouds would merge and become indistinguishable, due to the x, z warping. For the bare fiber, the distortions are mostly in the z direction, that is, out of the (approximate) plane of the shape; for the fiber in the guidewire, there is additional variation along x, that is, longitudinally.

The r.m.s. distance between the tip positions and their corresponding lattice positions for various fibers is summarized in Fig. 7. The inaccuracy is well below a millimeter. Analogous to the jitter, the variation around the lattice position is anisotropic, that is, different for different directions, and slightly larger for the fiber integrated in a device than for the bare fiber, and slightly smaller if the launch is fixed closer to the end of the fiber.

3.C. Tip orientation

Figure 8(a) shows the tip rotation angle measured using the FORS system, as a function of the known rotation of the mechanical stage that holds the fiber tip. There are two sets of curves in the Figure: colored curves show the twist derived by integrating the twist rate, and black curves show the orientation of the tip derived from tracking the locations of the outer cores. The latter takes into account geometrical

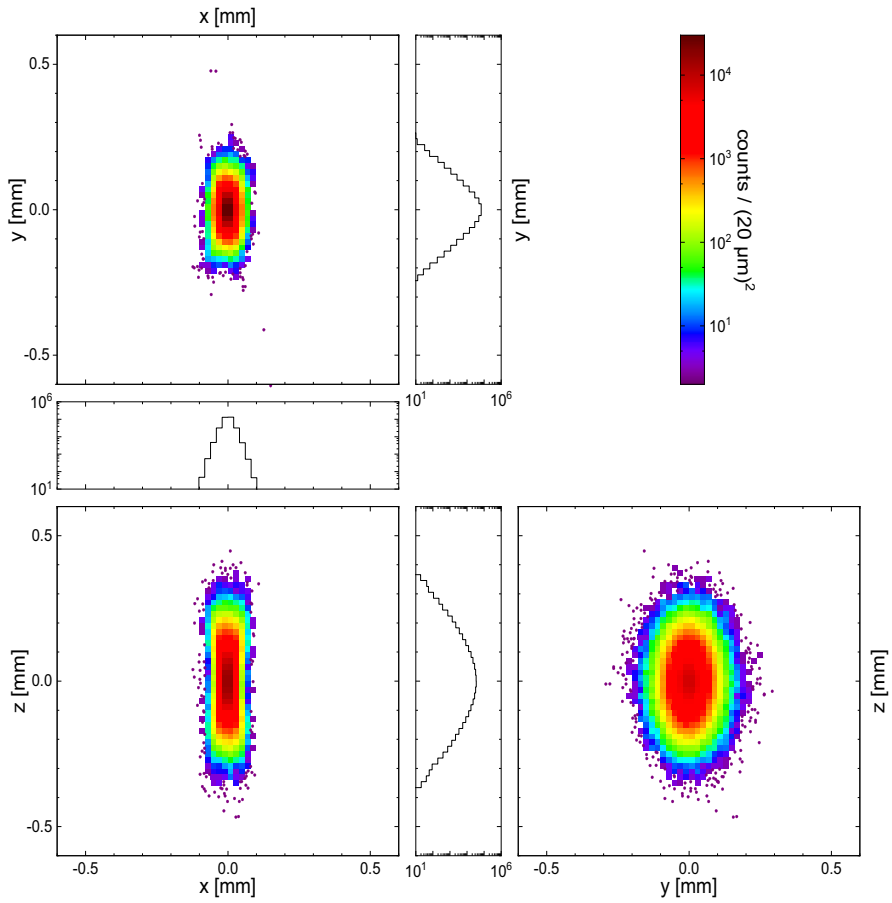

FIG. 4. Jitter of the tip of fiber SMB0168 around the average position, in three projections along principal axes, as two-dimensional histograms. The principal axes x', y', and z' are close to the directions of the axes x, y, and z in Figs. 2 and 3. Outliers are shown as separate markers. The launch at 50 cm from the tip. Axes are in millimeters. [Color figure can be viewed at wileyonlinelibrary.com]

contributions due to bending. The colored twist curves show considerable variation around the rotation angle. In contrast, the black curves faithfully track the angle from the stage; indeed the curves for the different fibers are indistinguishable from straight lines in Fig. 8(a). Figure 8(b) shows the difference between measured and requested rotation angles, that is, the residuals of the black curves in panel a. This makes the differences between various fibers visible. Table I summarizes the root-mean-square of these angular differences between the actual and measured rotation.

The rotation accuracies in Table I were measured with the fiber tip oriented parallel to the rotation axis of the stage. Interestingly, the fiber can also be oriented differently. Figure 9 shows accuracies for various angles between the fiber tip axis and rotation axis, for the SNA0003 fiber. For each orientation, the rotation measurements are repeated and the root-mean-square difference is reported in the Figure.

3.D. Path plate

The shape of the groove in the path plate is shown in Fig. 10. Also shown is the reconstructed shape of a fiber that was placed in the groove, but with the distance between fiber and groove magnified 50 times, to make small departures visible. Only two of the six fibers are shown, not to clutter the diagram. A different view of these distances is presented in Fig. 11, as a function of arc length along the fiber, for all six fibers. Figure 11(a) shows the out-of-plane component, that is, the seeming departure of the fiber from the plane of the path plate. To register the shape to the plane, the shape has been rigidly translated and rotated to minimize the largest out-of-plane distance. All six shapes always stay in the plane to within ± 1.2 mm, and the best one within 0.5 mm. The variations consist mostly of broad features extending over the full length of the shape.

The broad features in the out-of-plane distance contrast with the castellated features visible in the in-plane distance in Fig. 11(b), showing the in-plane distance to the closest point on the groove centerline, that is, transverse distance. The castellated features correlate with changes in curvature of the groove. For reference, the curvature is shown as a colored band in the figure. It turns out that the castellations are not an artifact of the reconstruction, but reflect the actual shape of the fiber in the groove. The groove is wider than the diameter of the fiber, so the fiber can relax its shape to some extent. Figure 12 shows that the transitions in curvature indeed are not as sudden for the fiber as compared with the groove. Returning to Fig. 10, we see that the fibers alternate between

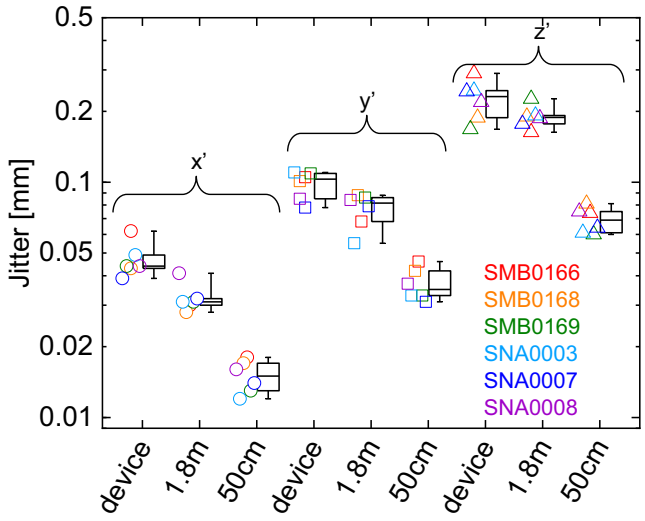

FIG. 5. "Jitter" of the tip position, for various fibers measured. The jitter is deduced from a hundred repeated measurements while the tip is held steady, and the variation is then averaged over the cube. The three components of the jitter (x', y', z') correspond to the principal axes that diagonalize the covariance matrix of the tip coordinates. These directions are close to the axes (x, y, z) in Figs. 2 and 3. The jitter has been measured in three situations: with fiber integrated in a 1.8 m long device (a guidewire); and with bare fiber, with a distance to the launch of 1.8 m, and with the launch closer to the tip, at 50 cm. The jitter for the long distance to the launch is larger than for the short distance, but not proportionately, since the shapes differ. [Color figure can be viewed at wileyonlinelibrary.com]

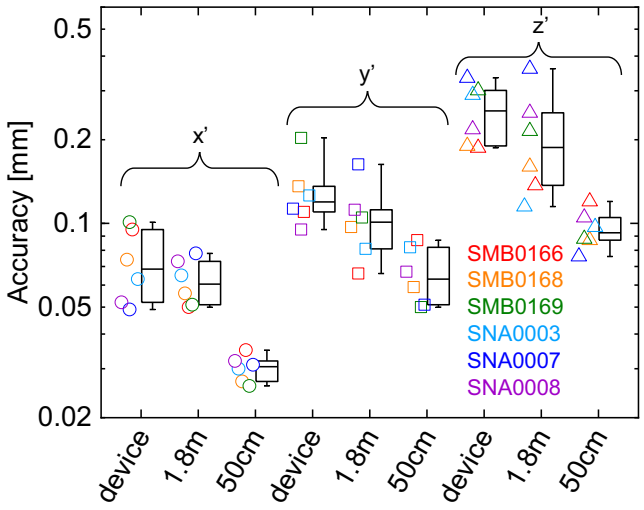

FIG. 7. Accuracies (r.m.s. distance between measured and actual lattice position) of a cubic lattice, measured with the launch at 50 cm and 1.8 m from the tip for a bare fiber, and for fibers integrated in a 1.8 m long guidewire. The three groups, labeled x', y', and z', correspond to the three principal axes of the error ellipse. [Color figure can be viewed at wileyonlinelibrary.com]

touching the inner and outer radii of the circular arcs that make up the groove shape. Due to the 50× lateral magnification, the transitions appear overly abrupt in Fig. 10; in reality, the transitions are smooth, of course. The inset shows a picture of the fiber in the groove at the end of the tight U-turn. The fiber can be seen transitioning to the other side of the groove here. The 0.4 mm diameter groove leaves generous clearance for the 0.2 mm diameter fiber. Since the distance to the centerline of the groove is plotted, the crossings of the fiber show up as transitions in Fig. 11(b). The 0.2 mm clearance matches with the height of the steps in the Figure. The longitudinal displacement of the fiber with respect to the groove (not shown) is consistent with this interpretation too, that is, the fiber gets ahead of the centerline after it "cuts corners."

The overall transverse distance variations are generally smaller than the out-of-plane variations, within ±0.9 mm for the six measurements shown, and usually smaller. Since these variations are generally of low spatial frequency, the root-mean-squared distance variations are only about half as big as the maximum departures. The departure of the reconstructed shape from the path plate shape is routinely measured as part of manufacturing of the fiber sensors, so this information is available for a much larger number of fiber sensors than the six fibers discussed so far. Figure 13 shows histograms of the maximum departure from the path plate shape over a length of 1.8 m, for well over 2300 bare fibers. The median of the maximum departure for each fiber is 0.72 mm out of plane, and 0.47 mm transverse, in-plane. The latter is perhaps most relevant for applications.

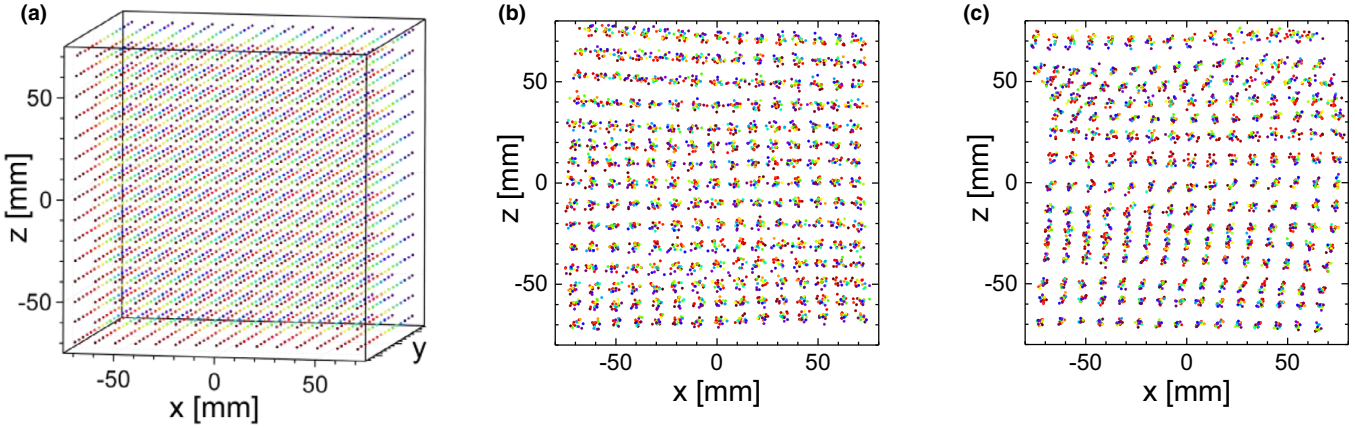

FIG. 6. Measured lattice positions, to scale (panel a), and with departures from the ideal lattice exaggerated 20× (panel b and c), for a typical bare fiber (SMB0168) with the launch at 1.8 m from the tip (panel b), and with the fiber integrated in a guidewire (panel c). [Color figure can be viewed at wileyonlinelibrary.com]

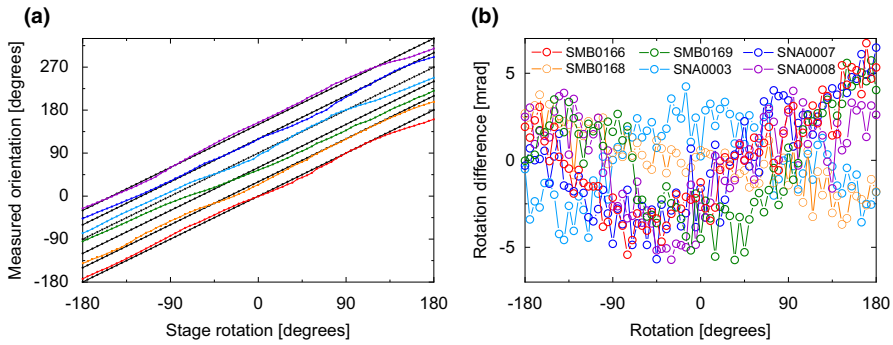

FIG. 8. Measured physical twist (panel a, colored curves) and measured orientation taking into account geometrical contributions due to bending (panel a, black curves) of the fiber tip vs angle of the rotation stage. Curves for various fibers have been offset by 30° for clarity. The physical twist itself is not in one-to-one correspondence with the stage rotation, but when bending is taken into account, then the curves straighten out and become indistinguishable from straight lines in panel a. The remaining small differences are shown in panel b. [Color figure can be viewed at wileyonlinelibrary.com]

TABLE I. Root-mean-squared difference between the shape-sensed rotation angle and the actual rotation angle from the rotation stage, for various fibers measured.

Fiber	$\Delta\vartheta$/ mrad
SMB0166	2.9
SMB0168	1.7
SMB0169	3.0
SNA0003	2.2
SNA0007	3.1
SNA0008	2.7
r.m.s.	2.6

The distance to the launch was 1.8 m. The last line summarizes the column above.

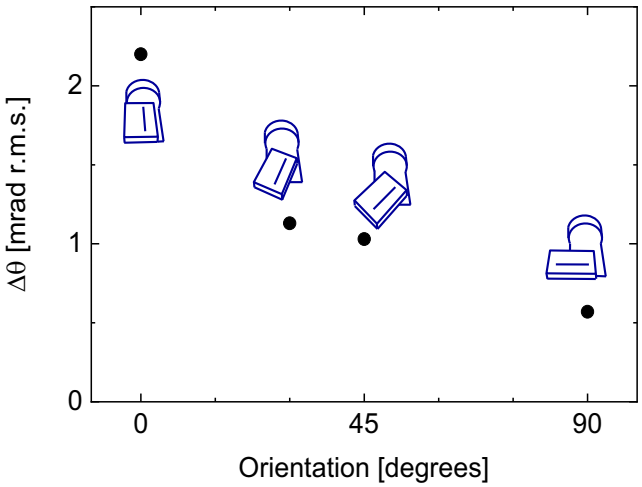

FIG. 9. Accuracy of rotation measurement depends on how the fiber tip is oriented with respect to the rotation axis, perpendicular (90°) is easier than parallel (0°). [Color figure can be viewed at wileyonlinelibrary.com]

4. DISCUSSION

The results for the jitter, distortion of the lattice, and rotation presented above, can be rationalized, as we will explain in the following sections. To close, we put the accuracy in the context of other shape sensing and tracking techniques.

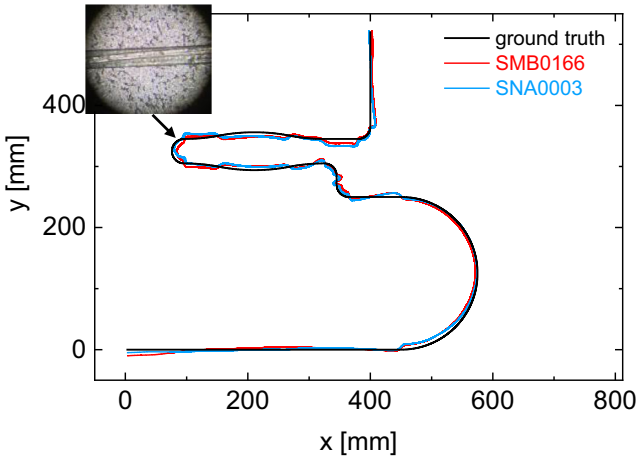

FIG. 10. Shape of the groove in a path plate (black curve), together with the reconstructed shapes of a fiber in this groove, for two different fibers (red and blue curves), with the departure from the actual groove shape magnified 50x. The fiber launch is at the bottom left, the tip at the top center. The reconstructed shape accurately tracks the shape of the groove; the slight departure shown by the red and blue curves is explained by the clearance between the fiber and the groove walls (see inset): the fiber does not follow the centerline of the groove, but alternates between touching the inner and outer radii to minimize its bending energy. [Color figure can be viewed at wileyonlinelibrary.com]

4.A. Jitter

The jitter has a quite a pronounced anisotropy, that is, it is different along the fiber and normal to or in the plane of the shape. This can be readily understood, knowing how the shape is calculated. The fiber length is determined with great precision, since the extension or compression is small to start with, and it is measured interferometrically. The accurately known length corresponds to the smallest component in the jitter. The two larger components have to do with bending. For a straight-line shape, the variations in measured bend strain would account for the jitter of the tip in the transverse directions, bending the shape away from the straight line. Twist would not matter—it would only rotate the fiber along its axis, without affecting the shape. The situation is different if there is a bend followed by a long more or less straight section. The straight section acts as an indicator pointer for any

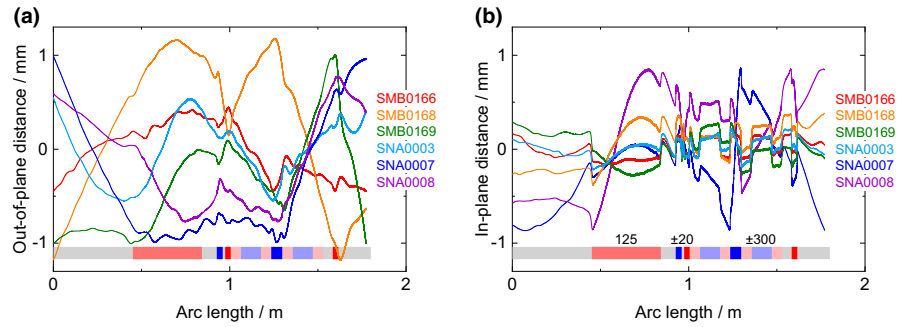

FIG. 11. Distance between the reconstructed fiber shape and the known shape of the groove centerline, vs arc length, split up into out-of-plane (panel a) and transverse in-plane (panel b) components. The color band shows the signed radius of curvature along the groove for reference, in mm. If you follow the fiber from launch to tip then curvature to the left is in red (positive), to the right is in blue (negative), with stronger curvature showing as more saturated color. [Color figure can be viewed at wileyonlinelibrary.com]

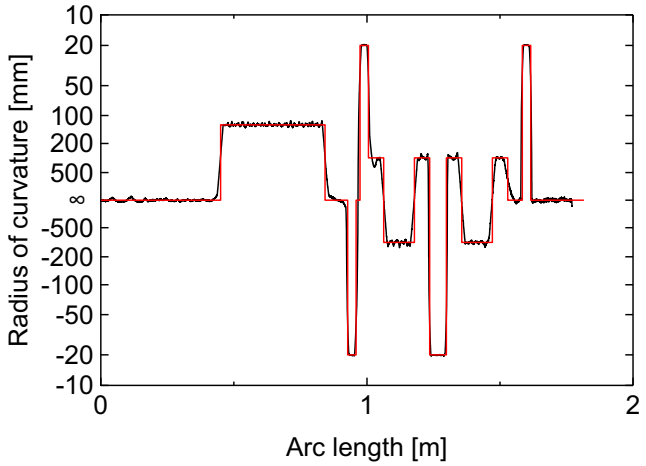

FIG. 12. In-plane curvature, along the fiber (as measured using SMB0166, in black) and along the center of the groove of the path plate (in red). (Note the quasi-logarithmic vertical scale.) The groove is wider than the fiber, so the fiber can relax its curvature. This is especially visible at the transitions between circular arc sections. [Color figure can be viewed at wileyonlinelibrary.com]

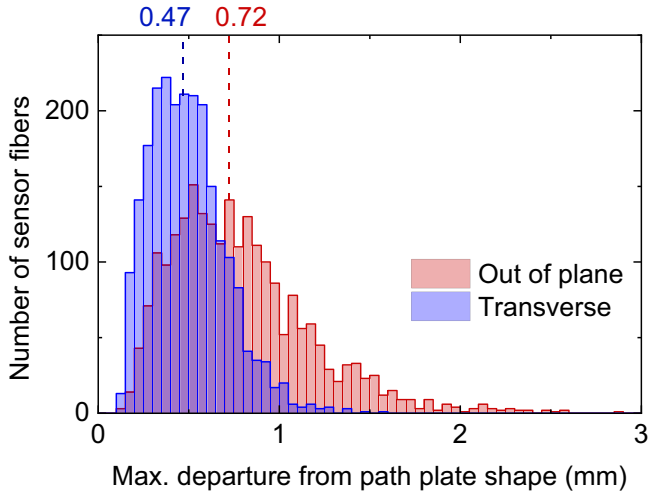

FIG. 13. Histogram of maximum departure of reconstructed shapes from the actual shape of the groove in the path plate, with over 2300 individual sensor fibers measured. Departure is measured as the shortest distance to the groove; it is separated into out-of-plane (red) and transverse (in-plane, blue) components. The dashed lines indicate the median of the distributions. [Color figure can be viewed at wileyonlinelibrary.com]

twist occurring proximal to the bend. The long arm amplifies small twist errors before the bend into large displacements distally, out of the plane of the bend. As a result, the jitter component out of the plane is larger than the in-plane jitter component.

Comparing different distances to the launch in Fig. 5, it appears that the jitter increases going from 50 cm to 1.8 m distance from the launch, which should not come as a surprise, since the tip position is the cumulative displacement of many small segments, each with their own variability. The more segments there are, the more these variations can accumulate. If the contributions of the segments were independent and identically distributed, then this reasoning would suggest that the variance in the tip position would scale with the length. However, the influence of the segments is not expected to be identical: a small change in direction at the beginning of a long arm will result in a large displacement of the tip. This would imply that the standard deviation rather than the variance of tip position should scale with the length; it could even vary more strongly than linearly, since not only the segment at the beginning, but also the intervening segments contribute (albeit with shorter arm). In our experiment, the jitter increases by a factor of ~2 going from 50 cm to 1.8 m distance from the launch, only slightly more than the $\sqrt{1.8/0.5} = 1.9$ lower bound. The arrangement with the launch close to the original position, looping the extra fiber back over the table, presumably helped avoid a large increase in arm, and avoid a larger increase in jitter.

For the fiber integrated in a device (a guidewire), we would expect the jitter to be unchanged, compared with the bare fiber with the launch at 1.8 m, since the length of fiber is the same. In Fig. 5, we see that the jitter tends to increase slightly when integrated; however, the increase is only barely significant, the variation in the jitter among the various fibers measured is comparable to the increase in jitter upon integration.

4.B. Tip positions

For the bare fiber, distortions are mostly in the z direction, since this direction is affected by twist the most. For the

curved shapes used (Fig. 3), the largest contribution to the uncertainty is due to the twist. For the fiber in the guidewire, the situation is different: the fiber is not fixed at the tip, only at the launch, so that it has freedom to rotate inside the guidewire lumen and should not accumulate twist or longitudinal strain when the surrounding guidewire is twisted or stretched. The downside is that the fiber can slightly shift inside its lumen. This adds uncertainty in the longitudinal direction, here along x. This is noticeable in Fig. 6(c).

The overall r.m.s. distance between tip positions and their corresponding lattice positions is summarized in Fig. 7. It closely follows the results for the jitter, perhaps not too surprising, since the same factors are at work. Nevertheless, it should be kept in mind that the accuracy depends on the shape, and the accuracies in Fig. 7 do not immediately generalize to arbitrary shapes, the figure just gives an indication of the achievable accuracy. Small curves in the proximal part of the fiber make the reconstruction more challenging; conversely, inaccuracies in the twist become less noticeable if the tip is in line with the twist axis. In particular, it can be seen that the accuracies in Fig. 7 do not scale proportionally with distance from the tip to the launch, as the shapes are different.

4.C. Tip orientation

The difference between measured and requested rotation angles, shown in Fig. 8(b), have little systematic structure, as desired. Table I summarizes the root-mean-square of these angular differences between the actual and measured rotation. This is larger than the accuracy of the rotation stage itself, which is guaranteed ± 0.5 milliradians. The attained relative accuracy of a few milliradians over a full turn, that is, better than 10^{-3}, is quite noteworthy, considering the substantial distance from the launch to the tip (1.8 m).

The rotation accuracy is reported for various relative orientations of the fiber tip and rotation stage, in Fig. 9. It turns out that the parallel orientation (0 degrees) as in Table I is the most unfavorable, that is, the test is the most stringent. This can be understood as follows. In the parallel orientation, the measured rotation depends crucially on the twist of the fiber itself. In contrast, if the axis of the fiber makes an angle with the axis of the rotation stage, then the measured rotation is determined substantially by the actual shape of the rest of the fiber, that is, by the curvature rather than the twist. Measuring bending accurately is easier than measuring twist accurately. Hence, the rotation accuracy is better when the axis of the fiber tip makes an angle with the axis of rotation.

4.D. In context

There are no standardized measurements reported on fiber optic shape sensing using OFDR. Duncan et al. showed 0.8 mm tip location accuracy over 1.1 m of sensed fiber,[9] using a predecessor of the current system. The earlier system used only three fiber cores, hence could not take into account twist. Galloway et al. investigated the possibility for sensing the planar surface shape accurately,[43] using a more recent system, also from Luna Innovations. Using 1.25 m of actively sensed fiber, a submillimeter accuracy is found. Parent et al. show application of OFDR based shape sensing in clinical practice.[44] Their custom system employs a Luna optical backscattering reflectometer with 1 Hz sampling rate, and three fibers glued together, rather than a single fiber with multiple cores. There is no provision for measuring twist. The reported accuracy is 2.8 ± 0.9 mm.

The accuracy of the tip location described here compares favorably with EM tracking results reported in literature.[1] The Wilson protocol for EM tracking also leads to r.m.s. accuracy results in the submillimeter range, when the fields are undistorted. However, when sources of magnetic distortion like a C-arm are present, the reported r.m.s. inaccuracy increases to multiple millimeters. In contrast to EM tracking, where the presence of magnetic or conductive materials can affect the fields, fiber optic shape sensing does not need interventional-environment dependent error compensation or per-procedure calibration. A review of EM tracking methods for endovascular navigation[2] shows that, when integrated into a medical device, the inaccuracy typically increases to multiple millimeters. Typically, these technologies only track the tip of the device; in contrast, the FORS technology provides the full shape.

5. CONCLUSIONS

We have investigated the precision and accuracy of tracking offered by Fiber Optic RealShape (FORS) technology. This shape sensing technology developed at Philips enables real-time tracking without line-of-sight restrictions. It achieves submillimeter precision, surpassing the reported precision of other navigation and tracking technologies. It provides information not just about the tip position and orientation, but about the full shape of devices in three dimensions as well. This provides superior visualization, potentially alleviating the need for fluoroscopy. It enables intuitive navigation and is expected to provide guidance to clinicians during minimally invasive procedures.

ACKNOWLEDGMENT

We acknowledge the support of and close cooperation with many colleagues in the FORS venture team in Philips.

CONFLICT OF INTEREST

The authors are employed at Philips Research and at Philips—Image Guided Therapy.

DATA AVAILABILITY STATEMENT

The data that support the findings of this study are available from the corresponding author upon reasonable request.

[a]Author to whom correspondence should be addressed. Electronic mail: mischa.megens@philips.com.

REFERENCES

1. Franz AM, Haidegger T, Birkfellner W, Cleary K, Peters TM, Maier-Hein L. Electromagnetic tracking in medicine—a review of technology, validation, and applications. *IEEE Trans Med Imaging*. 2014;33(8):1702-1725.
2. de Ruijter QM, Moll FL, van Herwaarden JA. Current state in tracking and robotic navigation systems for application in endovascular aortic aneurysm repair. *J Vasc Surg*. 2015;61(1):256-264.
3. Amanzadeh M, Aminossadati SM, Kizil MS, Rakić AD. Recent developments in fibre optic shape sensing. *Measurement*. 2018;128:119-137.
4. Henken KR, Dankelman J, van den Dobbelsteen JJ, Cheng LK, van der Heiden MS. Error analysis of FBG-based shape sensors for medical needle tracking. *IEEE/ASME Trans Mechatron*. 2014;19(5):1523-1531.
5. Froggatt ME, Klein JW, Gifford DK, Kreger ST, Inventors. Optical position and/or shape sensing. US8773650. 2014.
6. Froggatt ME, Duncan RG, Inventors. Fiber optic position and/or shape sensing based on Rayleigh scatter. US7772541B2.
7. Rice T. NASA-inspired shape-sensing fibers enable minimally invasive surgery. *Tech Briefs*. 2008.
8. Jansen M, Khandige A, Kobeiter H, Vonken EJ, Hazenberg C, Herwaarden Jv. Three dimensional visualisation of endovascular guidewires and catheters based on laser light instead of fluoroscopy with fiber optic real-shape technology: preclinical results. *Eur J Vasc Endovasc Surg*. 2020;60(1):135-143.
9. Duncan RG, Froggatt ME, Kreger ST, et al. High-accuracy fiber-optic shape sensing. *Sensor Systems and Networks: Phenomena, Technology, and Applications for NDE and Health Monitoring, Proceedings*. 2007;6530:65301S.
10. Tosi D, Schena E, Molardi C, Korganbayev S. Fiber optic sensors for sub-centimeter spatially resolved measurements: Review and biomedical applications. *Optical Fiber Technol*. 2018;43:6-19. https://doi.org/10.1016/j.yofte.2018.03.007.
11. Zhang L, Qian J, Shen L, Zhang Y. FBG sensor devices for spatial shape detection of intelligent colonoscope. Paper presented at: IEEE International Conference on Robotics and Automation, 2004. Proceedings. ICRA '04. 2004; 2004:843-840. https://doi.org/10.1109/ROBOT.2004.1307253
12. Yi X, Qian J, Shen L, Zhang Y, Zhang Z. An Innovative 3D Colonoscope Shape Sensing Sensor Based on FBG Sensor Array. 2007 International Conference on Information Acquisition; 2007:227-232. https://doi.org/10.1109/ICIA.2007.4295731
13. Park YL, Elayaperumal S, Daniel B, et al. Real-Time Estimation of 3-D Needle Shape and Deflection for MRI-Guided Interventions. *IEEE/ASME Trans Mechatron*. 2010:5607309.
14. Elayaperumal S, Plata JC, Holbrook AB, et al. Autonomous real-time interventional scan plane control with a 3-D shape-sensing needle. *IEEE Trans Med Imaging*. 2014;33:2128-2139.
15. Othonos A. Fiber Bragg gratings. *Rev Sci Instrum*. 1997;68(12):4309-4341.
16. Roesthuis RJ, Kemp M, van den Dobbelsteen JJ, Misra S. Three-dimensional needle shape reconstruction using an array of fiber bragg grating sensors. *IEEE/ASME Trans Mechatron*. 2014;19:1115-1126.
17. Borot de Battisti M, Denis de Senneville B, Maenhout M, et al. Fiber Bragg gratings-based sensing for real-time needle tracking during MR-guided brachytherapy: FBG-based sensing for needle tracking during MR-guided brachytherapy. *Med Phys*. 2016;43:5288-5297.
18. Sefati S, Pozin M, Alambeigi F, Iordachita I, Taylor RH, Armand M. A highly sensitive fiber Bragg Grating shape sensor for continuum manipulators with large deflections. Paper presented at: 2017 IEEE SENSORS; 2017; Glasgow. https://doi.org/10.1109/ICSENS.2017.8234018
19. Jäckle S, Eixmann T, Schulz-Hildebrandt H, Hüttmann G, Pätz T. Fiber optical shape sensing of flexible instruments for endovascular navigation. *Int J CARS*. 2019;14:2137-2145. https://doi.org/10.1007/s11548-019-02059-0
20. Gander MJ, MacPherson WN, McBride R, et al. Bend measurement using Bragg gratings in multicore fibre. *Electron Lett*. 2000;36:120.
21. MacPherson WN, Flockhart GMH, Maier RRJ, et al. Pitch and roll sensing using fibre Bragg gratings in multicore fibre. *Meas Sci Technol*. 2004;15:1642-1646.
22. Hou M, Yang K, He J, et al. Two-dimensional vector bending sensor based on seven-core fiber Bragg gratings. *Opt Express*. 2018;26:23770.
23. Khan F, Denasi A, Barrera D, Madrigal J, Sales S, Misra S. Multi-core optical fibers with bragg gratings as shape sensor for flexible medical instruments. *IEEE Sens J*. 2019;19:5878-5884.
24. Froggatt M, Moore J. High-spatial-resolution distributed strain measurement in optical fiber with Rayleigh scatter. *Appl Opt*. 1998;37:1735.
25. Childers BA, Froggatt ME, Allison SG, et al. Use of 3000 Bragg grating strain sensors distributed on four 8-m optical fibers during static load tests of a composite structure. *Proceedings Volume 4332, Smart Structures and Materials 2001: Industrial and Commercial Applications of Smart Structures Technologies*; 14 June 2001; Newport. https://doi.org/10.1117/12.429650
26. Parent F, Loranger S, Mandal KK, et al. Enhancement of accuracy in shape sensing of surgical needles using optical frequency domain reflectometry in optical fibers. *Biomedical Optics Express*. 2017;8:2210.
27. Westbrook PS, Kremp T, Feder KS, et al. Continuous multicore optical fiber grating arrays for distributed sensing applications. *J Lightwave Technol*. 2017;35:1248-1252.
28. Askins CG, Miller GA, Friebele EJ. Bend and Twist Sensing in a Multiple-Core Optical Fiber. Paper presented at: OFC/NFOEC 2008 - 2008 Conference on Optical Fiber Communication/National Fiber Optic Engineers Conference; 2008; San Diego, CA. https://doi.org/10.1109/OFC.2008.4528404
29. Lally EM, Reaves M, Horrell E, Klute S, Froggatt ME. Fiber optic shape sensing for monitoring of flexible structures. *Proceedings Volume 8345, Sensors and Smart Structures Technologies for Civil, Mechanical, and Aerospace Systems 2012*. 83452Y. 2012; San Diego, CA. https://doi.org/10.1117/12.917490
30. Werzinger S, Bergdolt S, Engelbrecht R, Thiel T, Schmauss B. Quasi-distributed fiber bragg grating sensing using stepped incoherent optical frequency domain reflectometry. *J Lightwave Technol*. 2016;34:5270-5277.
31. Idrisov RF, Varzhel SV, Kulikov AV, et al. Spectral characteristics of draw-tower step-chirped fiber Bragg gratings. *Opt Laser Technol*. 2016;80:112-115.
32. Waltermann C, Doering A, Köhring M, Angelmahr M, Schade W. Cladding waveguide gratings in standard single-mode fiber for 3D shape sensing. *Opt Lett*. 2015;40:3109.
33. Feng D, Zhou W, Qiao X, Albert J. Compact optical fiber 3D shape sensor based on a pair of orthogonal tilted fiber bragg gratings. *Sci Rep*. 2015;5:17415.
34. Soller BJ, Gifford DK, Wolfe MS. High resolution optical frequency domain reflectometry for characterization of components and assemblies. *Opt Express*. 2005;13(2):666.
35. Ding Z, Wang C, Liu K, et al. Distributed optical fiber sensors based on Optical Frequency Domain Reflectometry: a review. *Sensors (Basel)*. 2018;18(4):E1072.
36. Moore JP, Rogge MD. Shape sensing using multi-core fiber optic cable and parametric curve solutions. *Optics Expess*. 2012;20(3):2967-2973.
37. Herwaarden Jv, Jansen M, Bloemert-Tuin T, Borst GJD, Vonken E, Hazenberg CEV. *Innovation in 3D navigation: Results from the FORS - Fiber Optic RealShape first-in-human clinical study.* LINC. 2019. Available at: https://linc2019.cncptdlx.com/media/20190122_LINC_FINAL_JvH_PRESENTED.pdf. Accessed Nov 18, 2020.
38. Hazenberg S, Bloemert-Tuin T, Jansen M, Vonken EJ, Herwaarden Jv. *Fiber Optic Real Shape First-in-Human clinical study "Regular EVAR"*. Charing Cross International Symposium. 2019. Available at: https://www.youtube.com/watch?v=rVGWPwv4jq4&feature=youtu.be. Accessed Nov 18, 2020.
39. Kölbel T, Herwaarden Jv, Rohlffs F, Panuccio G. *Fiber Optic RealShape (FORS) Technology 3D-Device Guidance in Practice*. LINC. 2020. Available at: https://linc2020.cncptdlx.com/media/0900_Tilo_Klbel_29_01_2020_Room_2_-_Main_Arena_2_v1.pdf. Accessed Nov 18, 2020.
40. Wilson E, Yaniv Z, Zhang H, et al. A hardware and software protocol for the evaluation of electromagnetic tracker accuracy in the clinical

environment: a multi-center study. *Proc. of SPIE Medical Imaging: Visualization and Image-Guided Procedures*. 2007;6509:1-11.
41. Schönemann PH. A generalized solution of the orthogonal Procrustes problem. *Psychometrika*. 1966;31:1-10.
42. Kalman D. A singularly valuable decomposition: the SVD of a matrix. *College Mathematics J*. 1996;27(1):2-23.
43. Galloway KC, Chen Y, Templeton E, Rife B, Godage IS, Barth EJ. Fiber optic shape sensing for soft robotics. *Soft Robotics*. 2019;6(5):671-684.
44. Parent F, Gérard M, Monet F, et al. Intra-arterial image guidance with Optical Frequency Domain Reflectometry shape sensing. *IEEE Trans Med Imaging*. 2018;38(2):482-492.